Three-Dimensional Growth Modeling of the Healthy Radius and Ulna Using a Multi-Object Statistical Shape Model in Children

MSc Thesis Technical Medicine

Max van Zijderveld

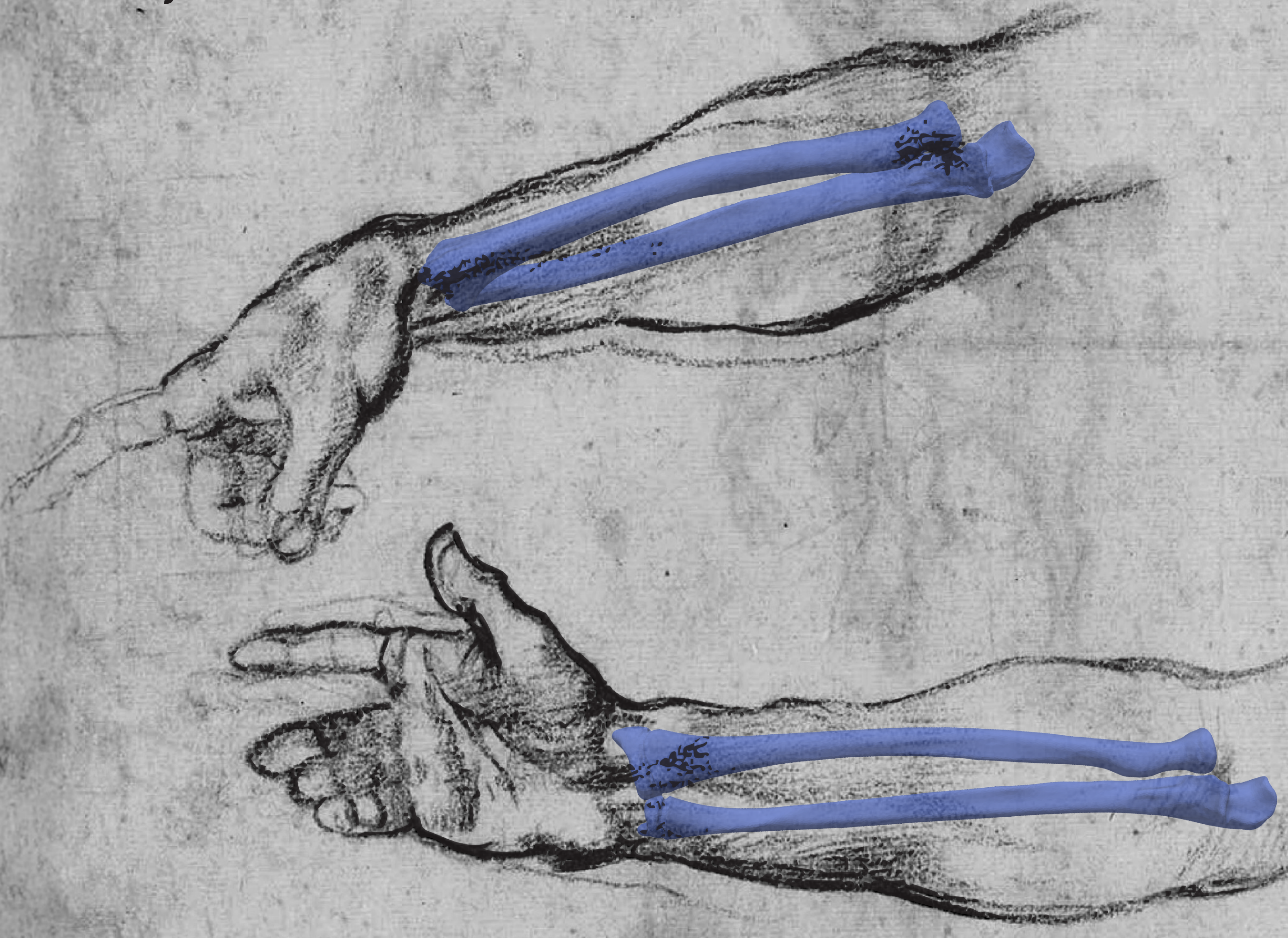

TU Delft

Erasmus MC
Universitair Medisch Centrum Rotterdam

Three-Dimensional Growth Modeling of the Healthy Radius and Ulna Using a Multi-Object Statistical Shape Model in Children

Max van Zijderveld

Student number: 4817982

July 1, 2025

Thesis in partial fulfilment of the requirements for the joint degree of Master of Science in

Technical Medicine

Leiden University - Delft University of Technology - Erasmus University Rotterdam

Master thesis project (TM30004 - 35 ECTS)
Dept. of Orthopaedics & Sports Medicine, Erasmus MC
January 2025 – July 2025

Supervisors

Dr. J.W. Colaris, MD	Medical supervision
Prof. Dr. H.E.J. Veeger	Technical supervision
D.F.R. van Loon, MSc	Daily supervision
E.M. van Es, MSc	Additional supervision

Thesis committee members

Prof. Dr. H.E.J. Veeger	TU Delft	Chair
Dr. J.W. Colaris, MD	Erasmus MC	
Dr. A. van Noort, MD	Erasmus MC	
E.M. van Es, MSc	Erasmus MC	

Abstract

Background

Fractures of the radius and ulna are common injuries in children, with improper healing potentially leading to limitations in forearm rotation affecting function and quality of life. Understanding the normal three-dimensional, age-related morphological variation and spatial relationship of the radius and ulna is essential to support clinical decision-making regarding surgical correction. Previous statistical shape models (SSMs) analyzed the radius and ulna separately, without considering their combined morphological and positional interaction during growth. This study aimed to develop a multi-object SSM of the pediatric forearm to capture combined age-related morphological and spatial variation and to compare its performance with single-object SSMs.

Methods

A cross-sectional dataset of 3D models of healthy pediatric forearms (n = 155; ages 3.8–18.8 years), reconstructed from computed tomography scans, was used to develop a multi-object SSM based on principal component analysis (PCA) and partial least squares regression (PLSR). The model captured the combined shape and position of both bones and enabled prediction of individual forearm geometry across ages during growth. Predictions were validated against follow-up scans of six participants. Morphological accuracy was assessed by root mean squared error (RMSE) and bone length error. Inter-bone spatial relationships were evaluated by comparing normalized distances and bounding box ratios between predicted and original meshes.

Results

The multi-object model captured age-related diaphyseal scaling and epiphyseal development. Absolute distance between the radius and ulna decreased with age, while their relative separation increased due to positional shifts. The PCA-based model achieved superior prediction accuracy (mean RMSE: 2.0 mm) compared to PLSR (3.5 mm). Morphological prediction accuracy was lower than that of single-object SSMs (mean RMSE: 2.4 and 1.7 mm vs. 0.9 and 1.0 mm). However, the multi-object model preserved inter-bone spatial relationships with good agreement longitudinally and reasonable consistency in transverse and sagittal dimensions.

Conclusion

While the multi-object SSM of the forearm does not outperform single-object models in predicting bone morphology, it enables combined modeling of morphology and spatial alignment. This approach provides additional insights into coordinated forearm development and may support future clinical applications in growth assessment and surgical planning.

Contents

1. **Introduction**

Fractures of the radius and/or ulna are among the most prevalent skeletal injuries in children [1-3]. Although pediatric bones have a natural ability to remodel deformities over time [4, 5], improperly or unbalanced healed fractures, referred to as malunions, can result in rotational limitations of the forearm. These limitations can impair daily functioning and quality of life [6-8]. If spontaneous correction does not occur, a corrective osteotomy may be required later in life to restore both the anatomical alignment and forearm function [9].

As it is currently not possible to predict the outcome of spontaneous correction, a thorough understanding of the normal three-dimensional (3D) growth patterns of the pediatric forearm is essential to support future clinical decision-making regarding surgical correction. This underscores the need for advanced 3D modeling techniques capable of accurately capturing and predicting both normal development and pathological deviations, such as those resulting from malunions.

Statistical shape modeling (SSM) has emerged as a promising technique for analyzing population-level anatomical variation. Prior studies have demonstrated that SSM can effectively describe age-related geometric variation and predict future bone morphology in single anatomical structures [10-12]. However, these so-called single-object SSMs are inherently limited, as they analyze bones in isolation and disregard the spatial and morphological interdependence between adjacent bones. For instance, although separate SSMs of the radius and ulna have been developed [13], they do not account for the coordinated development and positional relationship between these bones. This is a notable limitation, given that the functional anatomy of the forearm, especially its ability to rotate, critically depends on the interaction between the radius and ulna.

Functionally, the radius and ulna are unique bones, as their coordinated configuration enables rotational movement of the forearm, a rotational component not found elsewhere in the body. This rotation occurs at the proximal and distal radioulnar joints (PRUJ and DRUJ), where the bones articulate and move relative to one another. While single-object SSMs model each bone independently, they cannot capture the spatial relationship between the radius and ulna, especially at these joint interfaces. In this context, multi-object SSMs – which incorporate multiple anatomical structures simultaneously – offer a valuable alternative, as they explicitly represent inter-bone geometry and alignment.

This study aims to develop and evaluate a multi-object SSM of the pediatric forearm, based on computed tomography (CT) scans of healthy children, to characterize the combined morphological development of the radius and ulna during growth. By constructing a point distribution model (PDM) of both bones simultaneously, the model will capture shared patterns of age-related variation and represents the forearm as a single, integrated anatomical structure within a shared shape space. Whereas previous studies have modeled the radius and ulna separately, this study explores their coordinated geometric variation using conventional and widely adopted shape modeling techniques.

The research question guiding this study is:

- Does a multi-object SSM predict age-related variation in bone morphology more accurately than two single-object SSMs, and offer additional insight into the spatial relationship between the radius and ulna?

In this context, morphology refers to the shape characteristics of each bone individually. The spatial relationship refers to how the radius and ulna are positioned relative to each other.

2. **Methods**

2.1. Study Design

This study presents a descriptive analysis of age-related combined morphological and spatial variation of the radius and ulna during child development. Building upon prior single-object SSMs of the individual forearm bones, we aimed to develop a multi-object SSM that preserves and represents the anatomical relationship between the radius and ulna.

2.2. Data Acquisition and Study Population

We used a retrospectively compiled, cross-sectional dataset obtained from the research database of the Department of Orthopaedics at the Erasmus University Medical Center. The training dataset used to develop the multi-object SSM comprised 3D models of both radius and ulna from 155 participants, aged 3.8 to 18.8 years (mean: 13.3 years, SD: 3.3). These were reconstructed from segmented CT scans acquired between January 2017 and February 2025.

Only healthy forearms were included, originally scanned for comparison with the affected side in patients with various forearm pathologies. Scans with incomplete data were excluded. Demographic data, including sex and age at the time of scanning, were retrieved from the electronic health record. All data were fully anonymized and collected with participants' informed consent.

CT scans were acquired according to a standardized protocol using a fixation device to position the forearm in a functional neutral orientation, corresponding approximately to 0 degrees of pronation/supination. However, due to functional limitations associated with the underlying pathology (e.g., malunion), some patients were unable to achieve this position, resulting in varying degrees of pronation or supination.

The final cohort consisted of 86 males and 69 females, with 89 scans (57.4%) representing the right forearm. One-year follow-up (FU) scans were available for a subset of six participants from the training dataset (mean age: 13.9 years, SD: 3.1). These FU scans were used to validate the model's predictive performance and to enable comparison with the results of prior single-object SSMs of the forearm. Figure 1 illustrates the age and sex distribution of the study population, demonstrating a relatively balanced spread across the pediatric age range.

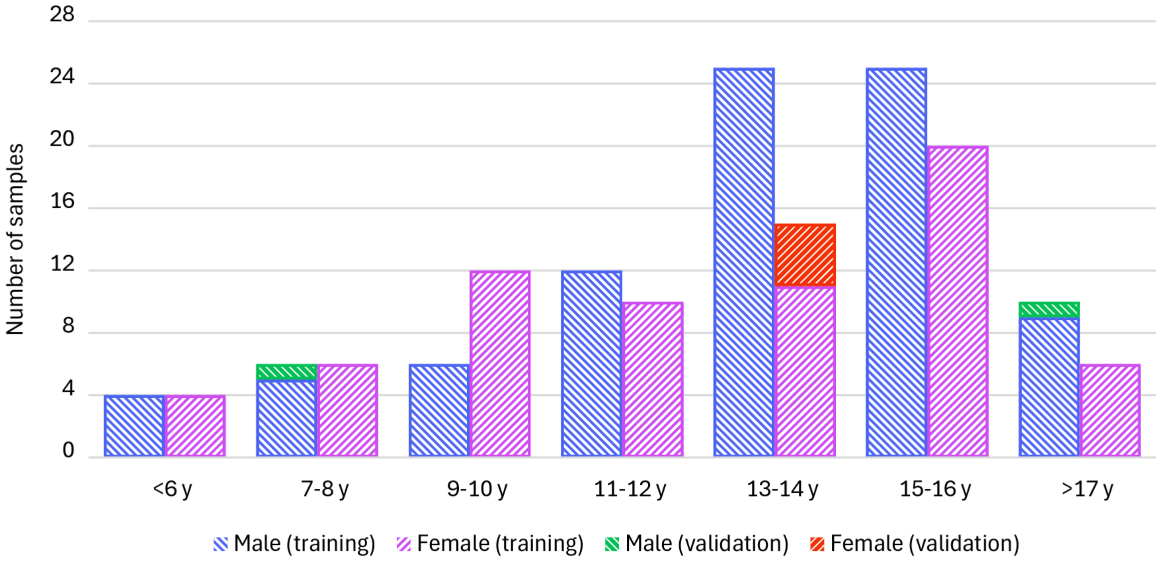

Figure 1. Age and sex distribution of the study population.

2.3. Data Preprocessing

All 3D models were checked to ensure they represented a single-body mesh. Multi-body meshes, typically due to unossified growth plates, were manually edited to produce unified geometries (Appendix A). Mesh quality was assessed using a Python script, which checked for the number of bodies, volume, watertightness, winding consistency, number of vertices and faces, and maximum edge length. To ensure consistent resolution across samples, all meshes were uniformly remeshed with a maximum edge length of 1.0 millimeter (mm).

2.4. Statistical Shape Model Development

The multi-object SSM was developed using Python (v3.9.13), ShapeWorks (v6.6.0-dev), and R (v4.5.0).

Unscaled data were used for modeling, following the previous study on single-object SSMs of the forearm, which demonstrated that age-related morphological variation is primarily driven by diaphyseal scaling and epiphyseal development [13]. Although scaling can be applied to eliminate inter-individual size differences and highlight more subtle shape variation, this approach has limited value in this pediatric cross-sectional dataset. In this context, growth-related variation in bone size explains such a large proportion of the total variance that more subtle morphological differences become negligible. Therefore, unscaled meshes were used in the present study.

2.4.1. Point Distribution Model

A PDM was constructed for both radius and ulna using a ShapeWorks-based Python script. Preprocessing included mirroring all left-sided 3D models to simulate uniform right-sided modeling. Laplacian smoothing (1 iteration, relaxation factor = 1.0) was applied to reduce surface noise while preserving morphological integrity. The *FillHoles* function was used to fill any mesh holes. All models were rigidly aligned to the ulna of an automatically selected reference model (i.e., the model closest to the population mean) using iterative closest point (ICP) registration (100 iterations), thereby eliminating translational discrepancies that could confound shape analysis.

PDM optimization was performed through iterative trial-and-error tuning of particle distribution parameters, aiming to achieve anatomically consistent point correspondences. Entropy-based particle splitting was employed to incrementally refine surface coverage [14]. The process began with a reduced particle count and dataset subset, which were gradually expanded to balance anatomical detail and computational efficiency. The final particle count was determined based on visual assessment of anatomical correspondence and diminishing improvements in geometric accuracy while maintaining computational feasibility.

The geometric accuracy of the final PDMs was evaluated via the average Euclidean distance between each particle and its nearest corresponding vertex on the original mesh, averaged across all samples. This metric reflects the reliability of particle-based shape representation.

2.4.2. Average Growth Model

To analyze the average geometric development of the radius and ulna over time, custom scripts were developed in R. Principal component analysis (PCA) and partial least squares regression (PLSR) were used to extract longitudinal growth trends from the cross-sectional dataset.

The mean shape PDM and corresponding mean meshes of the radius and ulna were exported from ShapeWorks Studio to enable reconstruction of age-specific 3D models.

2.4.3. Principal Component Analysis

PCA components were derived by decomposing the PDM into orthogonal modes that explain the greatest proportion of the combined shape variance. Since PCA components are not inherently time-dependent, linear regression was used to identify which components significantly correlated with age (significance threshold: $P \leq 0.05$).

The contribution of each principal component (PC) to the overall shape variation was quantified using the eigenvalues of the PCA, which represent the amount of variance explained by each component (compactness). The number of components retained for analysis was determined by a cumulative variance threshold of 97.5%, representing the point at which additional components contributed minimally to the overall explained variance. Two additional metrics were computed to evaluate model quality:

- *Generalization*, using a leave-one-out approach to quantify the model's capacity to represent unseen samples. This metric assesses how well the model generalizes to new data that were not included in the training set.
- *Specificity*, computed as the mean distance between synthetic samples generated by the model and their nearest sample in the training set. This metric assesses the realism of the generated samples by comparing them to the training set.

For each age, average shapes were predicted by linearly extrapolating age-correlated PCs. Non-significant PCs were fixed at their mean scores, thereby preserving interindividual structural variation without impacting age-related trends.

2.4.4. Partial Least Squares Regression

Unlike PCA, PLSR directly models the covariation between age and shape. Components were tested for correlation with age, and significant components were linearly regressed against age to generate growth predictions. Non-significant components were retained at their mean score.

2.4.5. Multi-Level Component Analysis

To distinguish shape variation within the bones from positional variation between them, multi-level component analysis (MLCA) was applied using the built-in functionality of ShapeWorks Studio. MLCA decomposes the total PCA variance into two orthogonal subspaces: one capturing intra-object morphological variation (shape), and the other capturing inter-object alignment variation (relative pose). The resulting shape and pose modes were visually explored within ±2 standard deviations (SD) to interpret their contributions to age-related variation.

2.4.6. Prediction Model

Model predictions based on PCA and PLSR were validated using the FU scans. All FU scans, both the original and the predicted meshes, were rigidly aligned to the ulna of the reference mesh using ICP registration. Only scans with comparable forearm rotation (i.e., pronation/supination) to their respective baseline scan were included, meaning that the FU scan was acquired with approximately the same degree of rotation, since the model does not correct for rotational variation.

Predictions were generated by projecting baseline PDMs onto the PCA or PLSR components to obtain individual scores. Age-correlated components were extrapolated using linear regression models, while non-age-correlated components retained their baseline scores. The final PDMs were reconstructed by multiplying component loadings with the updated scores and converting the resulting shape vectors back into 3D meshes.

To evaluate model performance, several outcome measures were defined. The primary outcome was the root mean squared error (RMSE) of per-vertex distances between predicted and original FU meshes. RMSE quantifies the average deviation across the bone surface and primarily reflects morphological prediction accuracy. Per-vertex error distributions were visualized by color-mapping onto the original FU meshes to identify regions with higher local error.

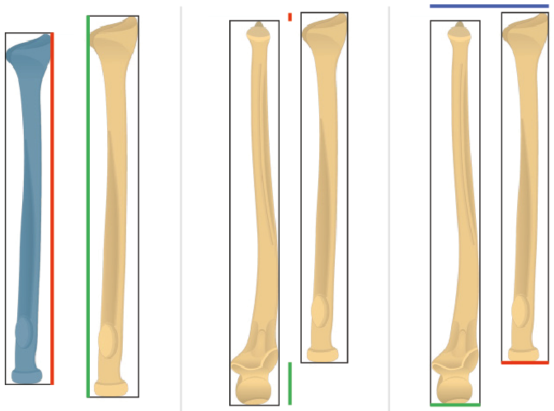

Figure 2. Visualization of bone length and inter-bone spatial measurements. The black lines indicate the bounding boxes used for length estimation. The left panel shows the absolute bone length of the predicted mesh (red line) and the original mesh (green line) for the radius. The middle panel displays the proximal (green line) and distal (red line) distances between the radius and ulna along the longitudinal axis. The right panel shows the widths of the bounding boxes in the Y direction: the total width including the articulating space between the bones (blue line) and the widths of the individual bounding boxes of the radius (red line) and ulna (green line).

Secondary outcomes included (Figure 2):

- The absolute difference in bone length for the radius and ulna individually, calculated by comparing the length of each predicted bone to the corresponding ground-truth mesh. Bone length was measured along the longitudinal (Z) axis as the longest dimension of the oriented bounding box.
- The ratio of the radial length to the ulnar length in each prediction compared to the original FU mesh. This measure indicates whether the relative proportion between the lengths of the radius and ulna is preserved.

- The relative spatial distance between the radius and ulna. To assess this, the distance between the bones along the longitudinal (Z) axis was measured at both the proximal and distal ends. These distances were then normalized to the length of the longer bone (ulna) within each configuration. This normalized metric enabled comparison of inter-bone positioning between predicted and original FU models and reflects the degree to which the spatial orientation of the radius relative to the ulna was preserved.
- Since an articulating space exists between the radius and ulna, the width of the axis-aligned bounding box (AABB) enclosing the combined radius-ulna complex (including this space) was measured. Separately, the widths of the individual AABBs of the radius and ulna were calculated. The ratio between the total width of the combined AABB and the sum of the individual widths was then compared between predicted and original configurations as a measure of preservation of the inter-bone spatial relationship. This approach enabled approximate quantification of the relative articulating space and assessment of whether the predicted models maintained the original spatial alignment of the radius and ulna along the X and Y axes.

Together, these measures allowed a quantitative assessment of morphological accuracy and an approximate evaluation of spatial fidelity. The same evaluation procedure was applied to the previously developed single-object SSMs to enable direct comparison of morphological performance, while the spatial measures provided an overall indication of whether the relative positioning between radius and ulna was preserved in the predictions of the multi-object model.

3. <u>Results</u>

3.1. Point Distribution Model

The constructed PDMs of the radius and ulna, each consisting of 2048 points, demonstrated dense point correspondence across all samples (Figure 3). Optimization parameters are summarized in Appendix B.

The mean geometric accuracy of the multi-object model was 0.37 mm (SD: 0.004), comparable to the single-object SSM, which achieved a mean accuracy of 0.35 mm (SD: 0.01).

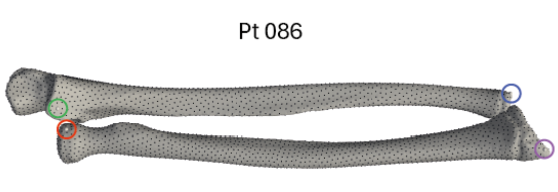

Figure 3. Visualization of point distribution models (PDMs) of the radius and ulna of different samples from the training set. Four particles are highlighted to illustrate the dense correspondence of the PDMs.

3.2. Average Growth Model

PCA- and PLSR-based average growth models were constructed from the PDMs for ages 4 to 18 years. Based on the cumulative variance threshold of 97.5%, the first five components of the PCA model accounted for 97.8% of the total shape variance, while the first six components of the PLSR model captured 97.5% (Figures 4 and 5). Generalization error decreased from 3.5 mm (1 PC) to <0.2 mm (154 PCs), and specificity reached a maximum of 2.7 mm (Figure 4).

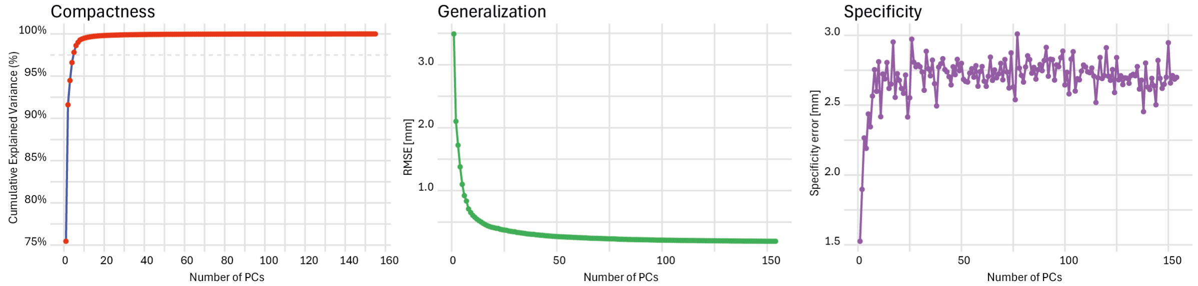

Figure 4. Model performance metrics for the principal component analysis (PCA) model. The dashed line indicates the cumulative variance threshold. PCs = principal components, RMSE = root mean squared error, mm = millimeter.

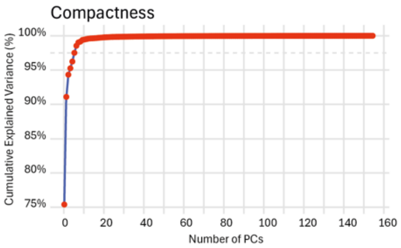

Figure 5. Model performance metric for the partial least square regression (PLSR) model. The dashed line indicates the cumulative variance threshold. PCs = principal components.

Correlation analysis showed that only the first principal component (PC1) in both models was significantly associated with age ($P \leq 0.05$) (Table 1) and was therefore used for age-related shape prediction. The remaining components, while explaining considerable shape variation, were fixed at their mean scores to preserve inter-individual variation without influencing the growth trend. Figure 6 shows the linear regression of PC1 against age.

Table 1. Significance (P-values) of the correlations between principal component analysis (PCA)/partial least square regression (PLSR) components and age. Significant P-values ($P \leq 0.05$) are highlighted in bold.

Principal Components	*PCA - P-value*	*PLSR – P-value*
PC1	**0.00**	**0.00**
PC2	0.14	0.14
PC3	0.19	0.16
PC4	0.88	0.17
PC5	0.80	0.07
PC6	-	0.10

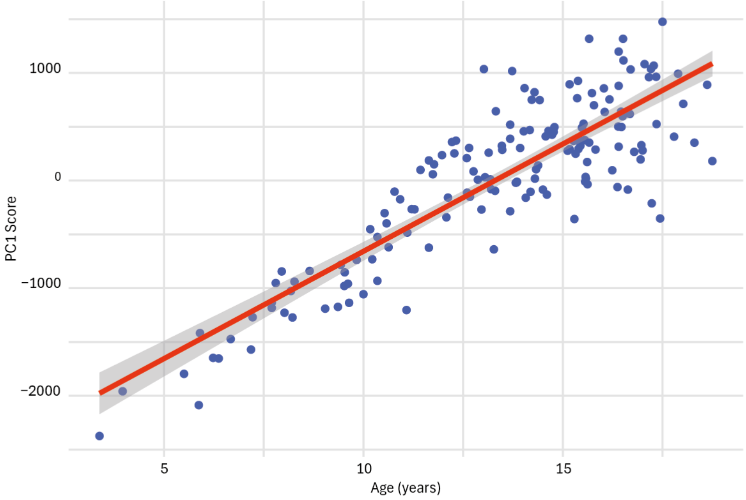

Figure 6. Linear regression of the first principal component (PC1) scores versus age.

To explore whether the growth trajectory across age could be more accurately described using a non-linear model, a second-order polynomial regression was also applied to age-correlated components. However, this approach did not improve prediction accuracy. Therefore, linear regression was retained as the primary method. Full results of the non-linear models are presented in Appendix C.

PC2, PC3, and PC5 showed significant correlation with scan orientation (i.e., pronation/supination) and were therefore excluded from interpretation as independent anatomical components (Table 2 and Appendix D).

Table 2. Significance (P-values) of the correlations between principal component analysis (PCA)/partial least square regression (PLSR) components and scan orientation. Significant P-values (P ≤ 0.05) are highlighted in bold.

Principal Components	*PCA – P-value*	*PLSR – P-value*
PC1	0.92	0.88
PC2	**0.00**	**0.00**
PC3	**0.00**	**0.00**
PC4	0.43	0.35
PC5	**0.00**	**0.03**
PC6	-	0.26

Reconstructed average shapes for ages 4 through 18 years are shown in Figure 7. The observed age-related shape variation primarily involved diaphyseal scaling and epiphyseal development, consistent with previous findings in single-object SSMs [13]. A new observation from this multi-object model was the reduction in absolute distance between the radius and ulna with increasing age, particularly at the PRUJ and DRUJ. This was visually observed as narrowing of the articulating space at these joint regions.

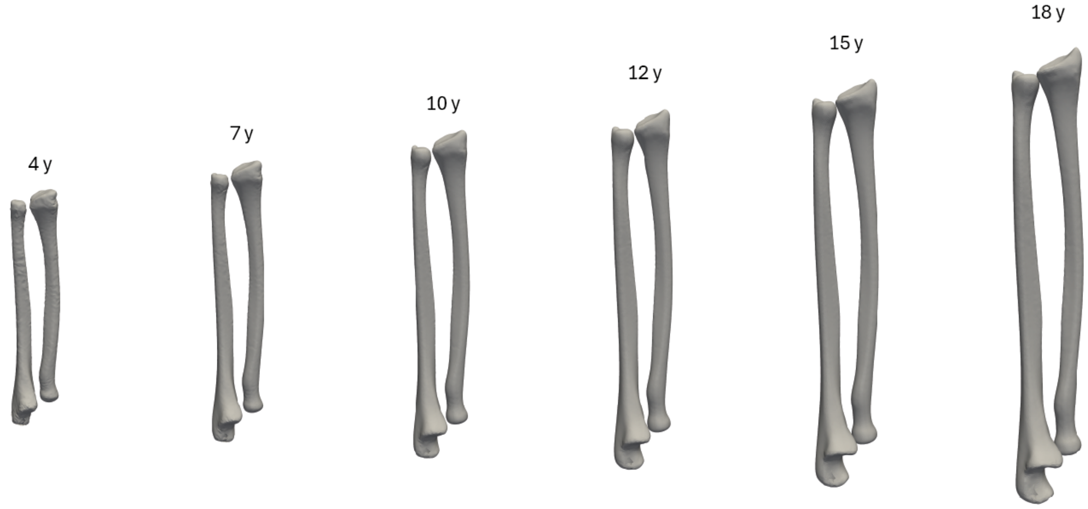

Figure 7. Predicted 3D forearm mean shapes at ages 4, 7, 10, 12, 15, and 18 years (y), based on the principal component analysis (PCA) model.

MLCA revealed that age-related variation in the pediatric forearm comprises both intra-bone shape variation and inter-bone positional shifts. The shape variation was dominated by diaphyseal scaling and epiphyseal development, while the pose variation captured spatial alignment differences between the radius and ulna. As the bones increase in size, they shift relative to one another in 3D space, leading to an increase in their relative distance, despite a decrease in absolute inter-bone spacing with age. Detailed MCLA visualizations are shown in Appendix E.

3.3. Prediction Model

The PCA-based prediction model achieved a mean RMSE of 2.0 mm (SD: 0.4), compared to 3.5 mm (SD: 1.6) for the PLSR model. For comparison with the single-object SSMs, the best-performing models for each method based on RMSE are presented in Table 3.

Table 3. Root mean squared errors (RMSE) for best-performing models. SSM = statistical shape model, mm = millimeter, SD = standard deviation.

	RMSE [mm] – radius	*RMSE [mm] – ulna*	*RMSE [mm] – radius + ulna*
Multi-object SSM	2.4 (SD: 0.6)	1.7 (SD: 0.4)	2.0 (SD: 0.4)
Single-object SSM	0.9 (SD: 0.2)	1.0 (SD: 0.3)	-

The mean absolute error in predicted bone length using PCA was 9.3 mm (SD: 7.7) for the radius and 9.3 mm (SD: 9.1) for the ulna, versus 7.9 mm (SD: 6.4) and 5.8 mm (SD: 5.3) respectively for PLSR (Appendix F). Despite slightly lower length errors in the PLSR model, PCA overall produced more anatomically plausible predictions. For reference, the single-object SSMs achieved substantially lower length errors: 2.8 mm (SD: 2.1) for the radius and 3.3 mm (SD: 2.8) for the ulna.

Figure 8 illustrates the worst-performing predictions based on RMSE for the multi-object models. In PCA predictions, errors primarily reflected differences in bone length, whereas PLSR predictions showed implausible deviations in the anatomical relationship between radius and ulna. Vertex-wise prediction errors for two of the best-performing validation samples are visualized as color maps in Figure 9, based on the PCA model.

Figure 8. 3D visualization of predicted versus original follow-up shapes (grey) for worst-performing cases, based on the principal component analysis (PCA) model (left) and partial least square regression (PLSR) model (right).

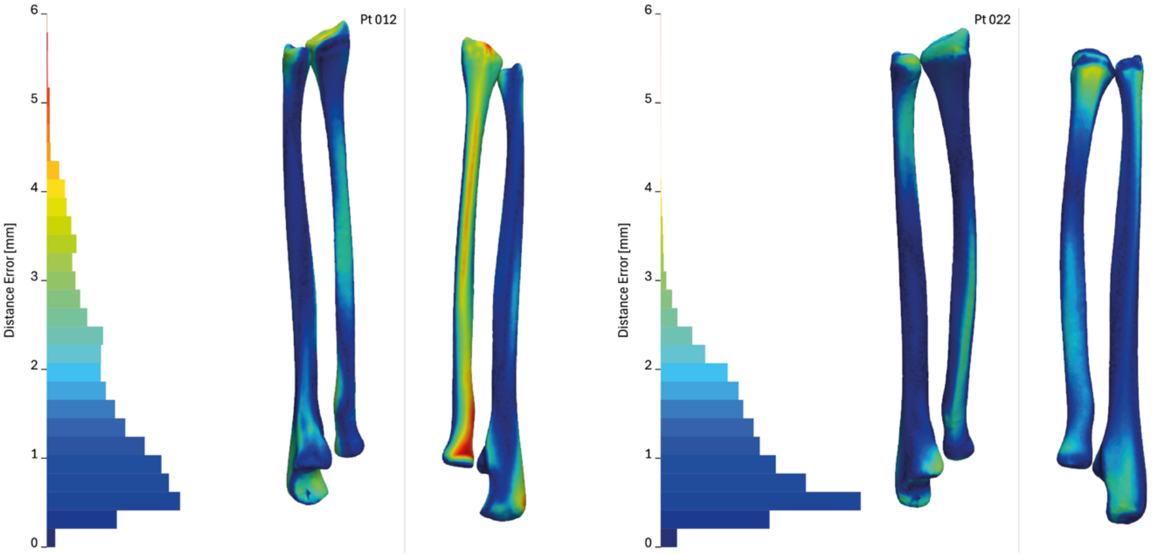

Figure 9. Vertex-wise distance error maps for best-performing prediction samples of the principal component analysis (PCA) model. A histogram with color legend is plotted on the left with the per-vertex distances in millimeter (mm).

Table 4 summarizes the differences in preserving the relative geometry of the radius and ulna for the best-performing models of each method. For the multi-object SSM, differences are reported for the ratio of radial to ulnar length, the normalized proximal and distal distances between radius and ulna, and the width ratios along the X and Y axes (reflecting relative articulating space). Since the single-object SSM does not capture inter-bone spatial relationships, only the bone length ratio is included for comparison.

Table 4. Differences in predicted ratios compared to follow-up (FU) meshes for the best-performing models. Δ = absolute difference between predicted and FU ratios, width ratio = ratio of the combined axis-aligned bounding box (AABB) width to the sum of the individual AABB widths, X and Y = axis direction.

	Ratio radial/ulnar length	*Δ Normalized proximal distance ratio*	*Δ Normalized distal distance ratio*	*Δ Width ratio (X)*	*Δ Width ratio (Y)*
Multi-object SSM	0.006 (SD: 0.003)	0.004 (SD: 0.005)	0.005 (SD: 0.004)	0.016 (SD: 0.011)	0.034 (SD: 0.021)
Single-object SSM	0.003 (SD: 0.001)	-	-	-	-

4. Discussion

4.1. Interpretation of the Results

This study presents 3D statistical shape models of the healthy pediatric forearm using multi-object SSM techniques based on PCA and PLSR. The resulting PDM achieved a mean correspondence accuracy of 0.37 mm, comparable to prior single-object models. Although corresponding particles did not always represent identical anatomical locations, this accuracy was sufficient to capture reliable age-related shape variation.

Age-related shape variation was primarily captured by PC1, the only component significantly associated with age. This component reflected diaphyseal scaling and epiphyseal development, which occur concurrently as part of coordinated bone growth. Smaller shape variations, such as internal rotations or subtle curvatures, may be clinically relevant at the individual level but were less prominent in this cross-sectional analysis, consistent with findings from single-object SSMs of the radius and ulna [13].

MLCA revealed that growth involves both intra-bone shape variation and inter-bone spatial realignment. Although the absolute distance between the radius and ulna decreased with age, their relative displacement increased at the level of the PRUJ and DRUJ, suggesting complex spatial interactions in coordinated development. The reduction in articulating space may reflect ossification of the interosseous cartilage during age-related development.

MLCA was used for anatomical interpretation only, not for prediction. It proved valuable in decomposing PC1 into distinct shape and pose components, illustrating relative displacement between the radius and ulna at the level of the PRUJ and DRUJ during growth. However, MLCA is not suited for growth prediction, since shape and posture need to be modeled simultaneously to preserve anatomical relationships. PCA-based multi-object models fulfill this by capturing coordinated shape and alignment variation.

The dataset included both meaningful (growth-related) and extrinsic (scan-induced) pose variation. Components PC2, PC3, and PC5 were retrospectively identified as representing scan position. MLCA's decomposition of these into shape and pose modes risked misinterpreting scan variability as anatomical change.

In comparing the multi-object methods, PCA produced more robust predictions, as reflected by a lower mean RMSE. While PLSR aims to identify components that jointly explain shape variation and age dependence, it may inadvertently capture irrelevant pose variation, leading to less accurate predictions. In contrast, PCA first models total shape variation and subsequently isolates age-related trends.

Validation with FU scans showed that PCA-based predictions, representing our best-performing multi-object model, were reasonably accurate, with a mean surface RMSE of 2.0 mm. Prediction errors were largest at the bone ends, especially around ages 12 - 14 years during the pubertal growth spurt, a phase marked by individual variation in growth rate and timing (Appendix F).

Only six FU scans were available, all acquired under standardized conditions using the fixation device. Despite this small number, they provided a reasonable estimate of model accuracy. Minor orientation mismatches remained between predicted and FU shapes, suggesting that the true RMSE values may be slightly lower than reported. This is visible in Figure 9, where *Patient 012* shows consistently offset along one side of the radius.

Compared to single-object SSMs, which showed lower RMSEs and smaller absolute bone length errors for the radius and ulna individually, the multi-object model did not improve morphological prediction accuracy. However, it enabled assessment of inter-bone spatial relationships, which were well preserved longitudinally and showed reasonable agreement in the transverse and sagittal planes. All comparisons were performed using the same six FU scans.

Prediction errors in inter-bone spacing may result from length prediction inaccuracies. When predicted bone length more closely matches an older or younger age than the original scan, the predicted spatial configuration shifts accordingly. This aligns with observed trends showing a reduction in absolute spacing with age. Improvements in bone length prediction could thus improve spatial accuracy.

4.2. *Strengths and Limitations*

For the first time, statistical modeling was applied to the full pediatric forearm. A strength of this study is the relatively large dataset, which exceeds the sample sizes of most prior multi-object SSM studies. Generalization and specificity were comparable to prior multi-object SSMs [15, 16]. Prediction accuracy was lower than in single-object models.

Fugit et al. [15] suggest that multi-object models can approach the accuracy of single-object models by retaining more components. However, our compactness analysis indicated diminishing returns in prediction accuracy with additional modes, highlighting the trade-off between generalization and specificity. While including additional modes could have further reduced generalization error and improved the model's ability to fit unseen samples, this would come at the cost of increased specificity error, indicating that generated shapes could deviate more from anatomically plausible forms.

One major methodological challenge was variation in forearm pose due to inconsistent scan positioning. The absence of, or inability to use, the fixation device during CT acquisition, often because of restricted forearm function due to malunion, resulted in differences in rotational alignment, such as pronation and supination. PCA showed that this pose variation was not isolated to a single component but was dispersed across multiple components (PC2, PC3, PC5). These components were correlated with each other, contradicting PCA's orthogonality principle. Although not age-dependent and thus excluded from the growth predictions, their presence complicates interpretation of shape variation.

Several approaches were explored to reduce pose-related variation and enable validation with randomly oriented scans. However, rigid alignment to the mean shape (scaled and unscaled models) using Procrustes analysis proved unsuccessful. This was particularly evident in older children, where alignment to the population mean shape (corresponding to approximately 12 years of age) resulted in anatomically implausible overlap between radius and ulna. Such alignment methods failed to account for the age-related increase in bone size and the associated separation of the forearm bones, as demonstrated by MLCA. This limitation of current alignment techniques in multi-object models is consistent with prior literature [15-22].

The current model provides valuable insights into average age-related variation but is not yet clinically applicable for tasks requiring high-precision predictions, such as corrective osteotomy planning. While small errors in overall bone length are unlikely to impair function if spatial alignment is maintained, the inter-bone spatial measurements used here, based on oriented bounding boxes, only approximate clinically relevant parameters. Because these boxes are not necessarily aligned identically for each bone, their dimensions do not precisely capture anatomical distances such as ulnar variance. In this analysis, the consistent orientation of predicted and original meshes allowed bounding box ratios to serve as a reasonable approximation. Additionally, predicting epiphyseal development remains particularly challenging, and small inaccuracies in this region can distort bone length estimation, as even minor shape deviations at the bone ends can lead to significant measurement errors when using bounding box-based length. Future studies should adopt more robust anatomical measures, for example by assessing ulnar variance or calculating minimal inter-bone distances at the PRUJ and DRUJ. Using anatomically defined landmarks would make these measurements more robust and clinically interpretable.

Prediction accuracy was lowest during the pubertal growth spurt. Although linear regression may oversimplify these non-linear growth trajectories, non-linear regression did not improve performance (Appendix C), suggesting that limitations may stem from PCA's reduced flexibility in capturing age-related variation within a multi-object space.

4.3. *Future Prospects*

Future improvements could include sex-specific modeling, reflecting known differences in skeletal growth patterns between boys and girls, which may also enhance non-linear growth predictions. Additionally, replacing chronological with skeletal age may increase predictive accuracy. In the long term, integrating longitudinal data, such as 3D reconstructions from low-dose biplanar EOS imaging, could enable personalized growth trajectories using mixed-effects modeling. Compared to CT, EOS allows for substantial radiation dose reduction, making it a more accessible and safer option for repeated imaging in children. This would facilitate the collection of longitudinal datasets needed for patient-specific forearm growth prediction.

More advanced methods, such as canonical powered partial least squares (CPPLS), may improve individual prediction by integrating multiple covariates, including age, sex, bone length, and scan position. Additional outcome measures aligned with radiological standards, such as ulnar variance or articular surface spacing, could further increase clinical relevance. While CPPLS has shown promise in single-object models, its performance in multi-object SSMs, where spatial relationships must be preserved, remains to be demonstrated.

A multi-object model holds potential for cases involving bilateral deformities, where no healthy contralateral reference is available. In such cases, the normal morphology of an affected bone (e.g., the radius) could potentially be inferred based on the geometry of its paired structure (e.g., the ulna). For such clinical applications, accurate modeling spatial relationships is essential, given their direct impact on forearm rotation.

An alternative approach to improve model performance would be to include only CT scans acquired with the fixation device. This would reduce the contribution of scan-position-related components and might reveal additional age-related modes currently masked by pose variability, ultimately leading to more accurate predictions. For example, one of the higher-order components (PC10) showed a non-linear correlation with age in the non-linear based PCA model and appeared to reflect variation in ulnar variance across the pediatric age range. This might relate to the asymmetric growth contribution of the distal radius and ulna, where approximately 75% of radial length growth occurs at the distal physis, compared to only 20% in the distal ulna [23]. However, this effect accounted for only a minor fraction of the total variance, likely because non-relevant variability from scan positioning explained a much larger proportion of the observed variation.

A promising direction is to correct for scan position retrospectively. Since rotation-related components (PC2, PC3, and PC5) significantly correlate with scan position, it may be possible to regress out or normalize their scores based on this correlation. This would enable more flexible model validation, even with randomly positioned scans.

Modeling of non-mature growth plates is a promising yet complex extension. In this study, non-ossified epiphyseal regions were synthetically attached to the bone, which may have limited the model's ability to capture ossification processes. Addressing this requires models that support a variable number of objects per sample, a technical frontier in multi-object SSM.

Although more powerful techniques exist, such as deep learning or non-linear manifold learning, this study deliberately employed conventional SSM methods (PCA and PLSR) due to their interpretability and methodological transparency. These methods are also consistent with prior multi-object SSM studies [15, 17-19, 21]. The more powerful approaches can model complex, non-linear relationships between age and shape variation that traditional linear methods may fail to capture. For example, deep learning can automatically learn hierarchical features from large datasets, while non-linear manifold learning methods such as kernel PCA better preserve local geometric relationships. In principle, these techniques could improve prediction accuracy. However, we considered it essential first to understand the anatomical and methodological challenges using established, transparent methods before exploring more complex alternatives.

4.4. Conclusion

In this study, we developed a 3D multi-object SSM of the healthy pediatric forearm, covering ages 4–18 years. While the model effectively captured age-related morphological variation within a shared shape space, its prediction accuracy was lower than that of single-object SSMs. However, the multi-object approach enabled assessment of spatial configuration, which was generally well preserved, particularly in the longitudinal direction. Although further refinement is required, this method provides added value for modeling coordinated forearm development and holds potential for future clinical applications.

5. References

1. Chung, K.C. and S.V. Spilson, *The frequency and epidemiology of hand and forearm fractures in the United States.* J Hand Surg Am, 2001. 26(5): p. 908-15.
2. Landin, L.A., *Epidemiology of children's fractures.* J Pediatr Orthop B, 1997. 6(2): p. 79-83.
3. Moon, R.J., et al., *Ethnic and geographic variations in the epidemiology of childhood fractures in the United Kingdom.* Bone, 2016. 85: p. 9-14.
4. Fuller, D.J. and C.J. McCullough, *Malunited fractures of the forearm in children.* J Bone Joint Surg Br, 1982. 64(3): p. 364-7.
5. Johari, A.N. and M. Sinha, *Remodeling of forearm fractures in children.* J Pediatr Orthop B, 1999. 8(2): p. 84-7.
6. Kasten, P., et al., *How does torsional deformity of the radial shaft influence the rotation of the forearm? A biomechanical study.* J Orthop Trauma, 2003. 17(1): p. 57-60.
7. Musters, L., et al., *Below-elbow cast sufficient for treatment of minimally displaced metaphyseal both-bone fractures of the distal forearm in children: long-term results of a randomized controlled multicenter trial.* Acta Orthop, 2021. 92(4): p. 468-471.
8. Musters, L., et al., *Does Early Conversion to Below-elbow Casting for Pediatric Diaphyseal Both-bone Forearm Fractures Adversely Affect Patient-reported Outcomes and ROM?* Clin Orthop Relat Res, 2024. 482(10): p. 1873-1881.
9. Roth, K., et al., *Accuracy of 3D Corrective Osteotomy for Pediatric Malunited Both-Bone Forearm Fractures.* Children (Basel), 2022. 10(1).
10. Ambellan, F., et al., *Statistical Shape Models: Understanding and Mastering Variation in Anatomy.* Adv Exp Med Biol, 2019. 1156: p. 67-84.
11. Cootes, T.F., et al. *Training Models of Shape from Sets of Examples*. in *BMVC92*. 1992. London: Springer London.
12. de Vries, L.E., et al., *Exploring shape changes in healthy bone growth through 3D spatiotemporal statistical shape models: A scoping review.* Bone Rep, 2025. 24: p. 101817.
13. de Vries, L.E., et al., *Growing InSight: Developing a 3D growth model for the healthy radius and ulna using statistical shape modeling*, in *Mechanical Engineering*. 2024, Delft university of technology.
14. Cates, J., S. Elhabian, and R. Whitaker, *Chapter 10 - ShapeWorks: Particle-Based Shape Correspondence and Visualization Software*, in *Statistical Shape and Deformation Analysis*, G. Zheng, S. Li, and G. Székely, Editors. 2017, Academic Press. p. 257-298.
15. Fugit, W.J., et al., *Accuracy tradeoffs between individual bone and joint-level statistical shape models of knee morphology.* Medical Engineering & Physics, 2024. 130: p. 104203.
16. Khan, N., et al., *Statistical multi-level shape models for scalable modeling of multi-organ anatomies.* Frontiers in Bioengineering and Biotechnology, 2023. 11.
17. Agrawal, P., et al., *Combined Estimation of Shape and Pose for Statistical Analysis of Articulating Joints.* Shape Med Imaging (2020), 2020. 12474: p. 111-121.
18. Audenaert, E.A., et al., *Separating positional noise from neutral alignment in multicomponent statistical shape models.* Bone Reports, 2020. 12: p. 100243.
19. Cerveri, P., A. Belfatto, and A. Manzotti, *Predicting Knee Joint Instability Using a Tibio-Femoral Statistical Shape Model.* Frontiers in Bioengineering and Biotechnology, 2020. 8.
20. Iyer, K., et al., *Statistical shape modeling of multi-organ anatomies with shared boundaries.* Frontiers in Bioengineering and Biotechnology, 2023. 10.
21. Peterson, A.C., et al., *Multi-level multi-domain statistical shape model of the subtalar, talonavicular, and calcaneocuboid joints.* Frontiers in Bioengineering and Biotechnology, 2022. 10.
22. Trentadue, T.P., et al., *Morphology of the scaphotrapeziotrapezoid joint: A multi-domain statistical shape modeling approach.* J Orthop Res, 2024. 42(11): p. 2562-2574.
23. Heeg, M. and W.L.M. Kramer, *Remodellering van fracturen bij kinderen.* Handboek Kindertraumatologie. 2006: de Tijdstroom.

6. **Appendices**

A: Growth Plate Attachment

Samples without an ossified growth plate, thus virtually identified as consisting of more than one body, were adjusted in Materialise 3-Matic and MeshLab (version 2023.12) to obtain one part.

We synthetically attached the proximal ulnar growth plate to the olecranon using the following process (Figure A1): (1) cutting the bone at metaphyseal height, (2) performing dilation followed by erosion on the epiphyseal part using uniform mesh resampling with a precision of 1 and an offset of ±7 mm, (3) merging the processed part and the original epiphyseal part, (4) merging the new one-bodied part with the original diaphyseal bone part.

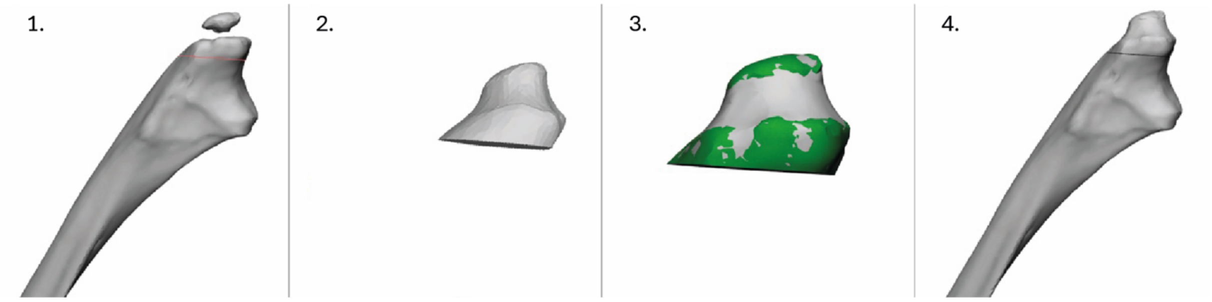

Figure A1. Visualization of the preprocessing steps to attach the growth plate to the ulna.

B: Optimization Parameters

Table B1. Parameters used for the point distribution model (PDM) optimization in ShapeWorks.

Initial Relative Weighting	0.1
Relative Weighting	20
Starting Regularization	1000
Ending Regularization	10
Iterations per Split	3000
Optimization Iterations	3000
Multiscale Start	32

C: Non-Linear Regression Model

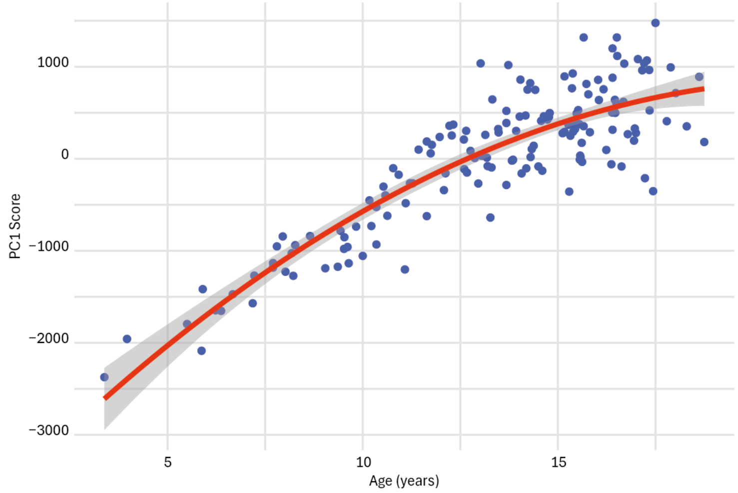

Figure C1. Non-linear regression of the first principal component (PC1) scores versus age.

Table E1. Extended results showing length differences of the radius and ulna for each follow-up participant, for both the non-linear principal component analysis (PCA) and partial least squares regression (PLSR) models. RMSE = root mean squared error, mm = millimeter.

Patient	*Age [years]*	*Sex*	*PCA - RMSE [mm]*	*PLSR - RMSE [mm]*	*Length difference radius PCA [mm]*	*Length difference ulna PCA [mm]*	*Length difference radius PLSR [mm]*	*Length difference ulna PLSR [mm]*
012	14.6	Female	1.9	2.3	-5.1	-3.0	-5.6	-3.8
013	18.3	Male	1.8	5.5	-13.8	-14.1	13.2	8.9
018	13.6	Female	2.1	3.2	-17.7	-20.3	2.8	-3.5
019	14.6	Female	3.1	2.2	17.3	16.3	5.2	3.0
022	8.5	Male	1.3	2.1	-2.7	-0.7	5.9	6.3
025	13.9	Female	2.7	5.0	11.2	13.6	11.0	7.8

Table E2. Extended results showing proximal and distal inter-bone distance between the radius and ulna for both predicted and original meshes of each follow-up participant, based on the non-linear principal component analysis (PCA) model. mm = millimeter.

Patient	*Proximal distance – predicted [mm]*	*Distal distance – predicted [mm]*	*Proximal distance – original [mm]*	*Distal distance – original [mm]*
012	28.9	11.2	27.7	13.6
013	31.6	6.4	32.4	6.7
018	28.3	5.9	30.8	7.0
019	30.1	8.9	28.5	5.6
022	22.0	4.9	19.5	6.0
025	28.4	9.1	27.1	9.1

Table E3. Differences in predicted ratios compared to follow-up (FU) meshes for the non-linear principal component analysis (PCA) model. Δ = absolute difference between predicted and FU ratios, width ratio = ratio of the combined axis-aligned bounding box (AABB) width to the sum of the individual AABB widths, X and Y = axis direction.

Ratio radial/ulnar length	*Δ Normalized proximal distance ratio*	*Δ Normalized distal distance ratio*	*Δ Width ratio (X)*	*Δ Width ratio (Y)*
0.007 (SD: 0.003)	0.004 (SD: 0.005)	0.005 (SD: 0.004)	0.016 (SD: 0.010)	0.033 (SD: 0.023)

D: Scatterplots of Scan Orientation-Correlated Components

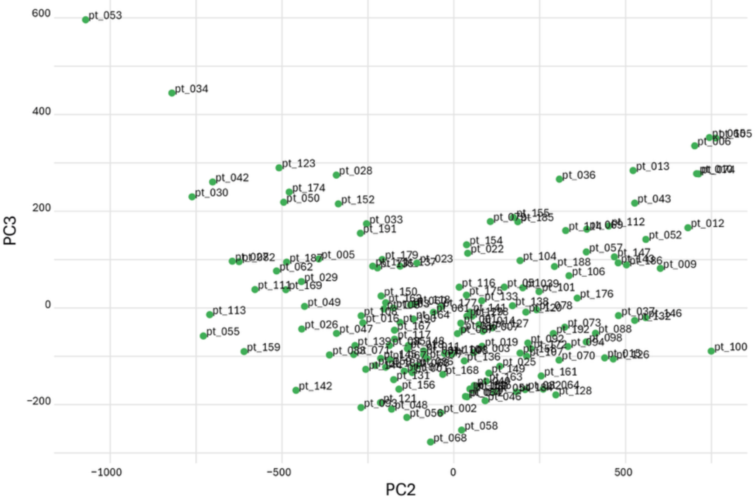

Figure D1. Scatterplot of the second and third principal components (PC2 and PC3) from the PCA model, illustrating the distribution of shape variation across the dataset.

E: Multi-Level Component Analysis Result

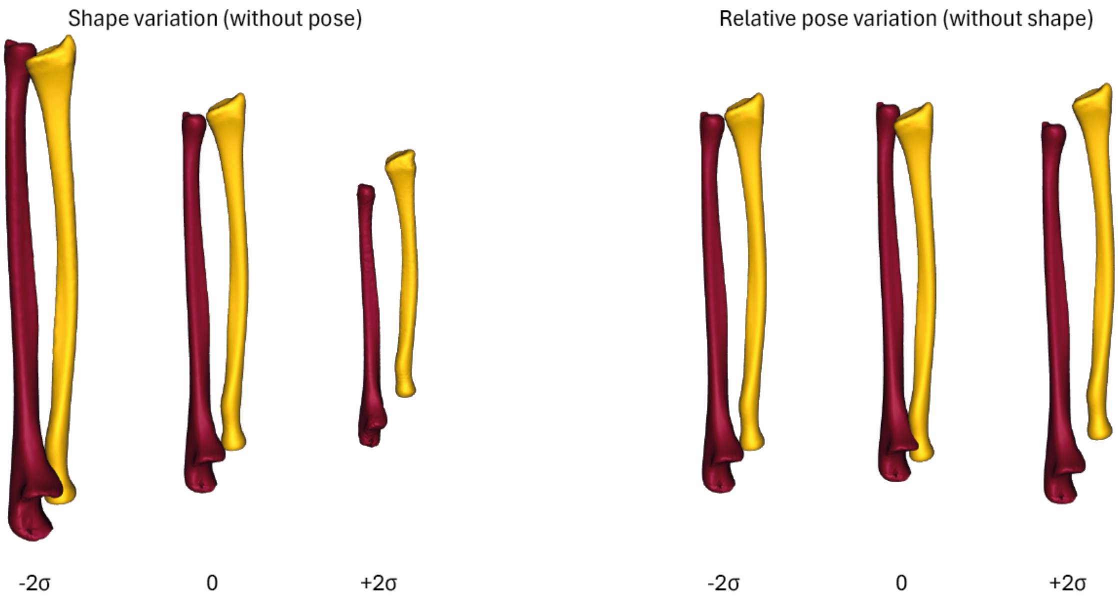

Figure E1. Visualization of variations along the first principal component from the multi-level component analysis (MLCA), shown within ±2 standard deviations (σ) from the mean shape.

F: Additional Results of Prediction Model

Table F1. Extended results showing length differences of the radius and ulna for each follow-up participant, for both the principal component analysis (PCA) and partial least squares regression (PLSR) models. RMSE = root mean squared error, mm = millimeter.

Patient	*Age [years]*	*Sex*	*PCA - RMSE [mm]*	*PLSR - RMSE [mm]*	*Length difference radius PCA [mm]*	*Length difference ulna PCA [mm]*	*Length difference radius PLSR [mm]*	*Length difference ulna PLSR [mm]*
012	14.6	Female	1.9	2.3	-7.8	-5.9	-4.1	-1.7
013	18.3	Male	2.0	5.9	-1.8	-1.4	18.6	14.4
018	13.6	Female	2.2	3.2	-22.3	-25.2	3.7	-2.4
019	14.6	Female	2.6	2.4	14.1	13.3	7.1	5.2
022	8.5	Male	1.3	2.1	-2.7	-0.7	1.5	1.3
025	13.9	Female	2.2	5.1	7.4	9.1	12.2	9.2

Table F2. Extended results showing proximal and distal inter-bone distance between the radius and ulna for both predicted and original meshes of each follow-up participant, based on the best-performing model. mm = millimeter.

Patient	*Proximal distance – predicted [mm]*	*Distal distance – predicted [mm]*	*Proximal distance – original [mm]*	*Distal distance – original [mm]*
012	28.5	11.1	27.7	13.6
013	33.1	7.1	32.4	6.7
018	27.9	5.4	30.8	7.0
019	29.9	8.7	28.5	5.6
022	22.0	4.9	19.5	6.0
025	27.7	8.8	27.1	9.1